3

Redox Switching Behaviour in Resistive Memory Device Designed Using a Solution-Processable Phenalenyl-based Co(II) Complex: Experimental and DFT-Studies

Research Article:
Kamboj, N., Betal, A., Majumder, M., Sahu, S., and Metre, R. K., (2023), "Redox Switching Behavior in Resistive Memory Device Designed Using a Solution-Processable Phenalenyl-Based Co(II) Complex: Experimental and DFT Studies", *Inorganic Chemistry*, Vol.62, No.10, pp.4170–4180.

3.1 Introduction

The extensive innovations in electronic devices owing to the physical and theoretical limits of traditional silicon-based information storage have directed the expansion of next-generation data storage devices in the last two decades [Tan et al., 2015]. The modern semiconductor industry demands electronic devices that offers easy fabrication, portability, high endurance, and a storage device with technology that reserves its data even when the power is disrupted [Zhao et al., 2018]. Memristors or resistive random access memory(RRAM) are one of the promising contenders, actively researched and continuously being developed for the non-volatile memory(NVM) [Ji et al., 2016; Yang et al., 2013, 2009]. The non-destructive resistance change modulated in the memristor devices by the electrical stimulus is proved to offer high scalability, multi-bit storage potential and high speed for the operation to obtain a diverse range of switching behaviours [Jo et al., 2008; Lin et al., 2014].

Organometallic and transition-metal complexes(TMCs) have been widely employed as active materials in resistive memory switching devices and evaluated as potential component for modern-day electronics [Barman et al., 2021; Kandasamy et al., 2018; Li et al., 2020; Mishra et al., 2020, 2021]. A well-defined coordination environment, reversible redox behaviour and the interplay between metal ions and the organic ligands [Barman et al., 2019] make them advantageous for obtaining the bi- or multi-states in the RRAM devices in contrast to the traditional silicon-based memory devices offering conventional binary memory states [Bandyopadhyay et al., 2011; Shao et al., 2019]. In this context, Goswami and coworkers have reported a resistive memory storage device based on the active layer of a Ruthenium-coordinated azo-aromatics complex with a robust switching process between two resistive states with high reproducibility, fast switching and scalability(down to ~60 nm^2) [Goswami et al., 2017]. Another seminal work in this direction by Hong and coworkers reported the solution-processable fabrication of resistive memory devices based on the phosphole oxide-containing alkynylgold(III) complex as an active layer [Hong et al., 2016]. Recently, Barman and coworkers designed a write once-read many(WORM) type resistive storage device based on a Cobalt(II) complex [Barman et al., 2021]. Kandasamy and coworkers fabricated various polypyridyl Cr(III) complexes based RRAM devices and observed that the variation in the coordination sphere by changing the ligand design lead to the difference in ON/OFF ratio (10^4–10^6) [Kandasamy et al., 2018]. The latest report by Shao and coworkers reviewed the significant role of a ligand design in controlling molecular switching in TMC-based memory devices [Shao et al., 2019].

TMCs derived from electro-active phenalenyl-based ligands are well known in the literature [Dale et al., 2019; Dey et al., 2012, 2013; Kamboj et al., 2022; Kubo, 2015; Mukherjee et al., 2017; Pariyar et al., 2015; Wahl et al., 2019b]. Haddon in 1975, introduced the importance of phenalenyl(PLY) molecule in the modern semi-conductor industry and regarded PLY as one of

the graphene fragment [Haddon, 1975]. The past studies have made it evident that the delocalized carbon-based charged species with unpaired spin in PLY redox motif have exhibited many promising molecular device properties [Ahmed et al., 2021; Bhunia et al., 2019a; Haddon et al., 2008; Huang et al., 2003; Raha Roy et al., 2014]. Raman and coworkers used the zinc(II) metal ion complex containing a cationic PLY unit as an electro-active material for constructing a spin-based memory device [Raman et al., 2013]. The control of redox properties by slight modifications in the delocalized PLY-derived ligands and their coordination with metal ions can help synthesize new materials for storing the information. Therefore, PLY, and its derivatives are important multifunctional molecules from the device physics point of view [Kubo, 2015]. In this context, herein, we report a new electro-active [$Co^{II}L$] complex, **1**, obtained using PLY-based ligand LH_2, *9,9'-(Ethane-1,2-diylbis(azanediyl))bis(1H-phenalen-1-one),* the device fabrication and its performance in resistive switching memory. The present molecular design with a non-precious metal, and a redox-active PLY ligand has opened up the scope for the utilization of intriguing PLY ligand's non-bonding molecular orbital (NBMO) into the redox-switching pathways. Compared to the earlier reports with precious heavy metals, such as ruthenium and gold, the present approach describes a plausible mechanism where the SOMO orbital of the complex **1** is involved in initiating the charge-transfer process, hence, the over-all stability of the molecule during the device performance tests is not compromised. In addition to that, the interesting π-π stacking of phenalenyl groups in the ligand system is anticipitaed to cause substantial intermolecular overlap of the molecular orbitals, that favours easy intermolecular charge transfer in the solid state. The same observation is supported by the corresponding DFT studies. Further, the ITO/$Co^{II}L$/Al device has interestingly shown a low voltage switching (0.3 V) that supports the facile electron transport between the complex **1** and the electrodes utilised to fabricate the device. The redox mechanistic pathway for the observed low-voltage switching behaviour has been explained with the help of detailed electrochemical characterization and DFT studies.

3.2 Experimental Section

3.2.1 Synthesis of [$Co^{II}L$] Complex, 1

A solution of $Co(OAc)_2 \cdot 4H_2O$ (48mg, 0.24 mmoles) in 5ml of ethanol was slowly added to the suspension of LH_2 (80mg, 0.24 mmoles) in ethanol (30ml) under nitrogen atmosphere. The reaction mixture was refluxed for 24 hours resulting in the formation of dark green precipitate. The precipitate thus obtained was filtered and washed subsequently with ethanol. The precipitate was dissolved in DCM/benzene (1:1) solvent mixture, which on slow evaporation, resulted in X-ray quality dark green crystals of the complex **1**. Yield (based on Co): 60 mg (62%). FT-IR (KBr discs) ν(cm^{-1}): 420(m), 686(m), 832 (s), 1240(s), 1586(s), 1632(s), 3045(m). UV-vis (DCM) λ/nm (ε in $M^{-1}cm^{-1}$): 285(28087), 344(20639), 477(24344), 621(14514). Elemental analysis: Anal. Calcd. for $C_{28}H_{18}CoN_2O_2$: C, 71.04; H, 3.83; N, 5.92. Found: C, 71.56; H, 4.006; N, 5.96. HRMS (positive, CH_3CN) m/z = 473.07 $(M)^+$.

3.2.2 Computational Details

The Density Functional Theory (DFT) and Time-Dependent Density Functional Theory (TD-DFT) computations were performed using the ORCA 5.0.2 programs.[Neese et al., 2020a] The geometry of [$Co^{II}L$] complex,**1** was optimized by using a GGA functional BP86 method in conjugation with a basis set def2-TZVP[Weigend et al., 2005a] on ligands (C, H, O, N) and a small core effective core potential (ECP) with the corresponding valence basis set on the metal atom (Co), namely LANL2DZ.[Hay et al., 1985; Roy et al., 2008] To improve the computational speed, the RI approximation[Kollmar et al., 2019b] with a combination of an auxiliary basis set (def2/J)[Weigend, 2006a] was also employed in all spin-unrestricted DFT and TD-DFT calculations. No symmetry restrictions (i.e. C1) were held during the geometry optimizations. Frequency analysis calculations were performed to verify the minimum character of all

optimized structures (no imaginary frequency). The resultant geometries from optimization were used in subsequent single-point energy and TD-DFT calculations at the BP86/def2-TZVPP level of theory along with Grimme's dispersion correction, D3BJ.[Allouche, 2012; Grimme et al., 2010b] The Natural Population Analysis (NPA), Wiberg Bond Index (WBI) value and Natural Bond Order (NBO) analysis were performed at the same level of theory (BP86+D3BJ/def2-TZVPP//BP86/def2-TZVP+LANL2DZ). The NBO 7.0[Glendening, 2018] program interfaced with ORCA 5.0.2 program was used for the present study. The solvent effect in TD-DFT calculations was considered by using the CPCM method[Barone et al., 1998a] with dichloromethane (DCM). Avogadro software[López, 2014] was used for the visualization of molecular orbitals and spin density.

3.2.3 Device Fabrication

A metal-insulator-metal (MIM) structured device, ITO/Co^{III}L/Al was prepared with the newly synthesized [Co^{III}L] complex, **1** as an active layer, and Al and ITO as the top electrode (TE) and bottom electrode (BE), respectively. Before fabrication, the glass substrate was cut into small pieces of area 1.5 cm× 1.5 cm. The substrates were cleaned with soap solution, acetone, ethanol, and DI water by ultra-sonication for 15 minutes each as reported previously. After ultra-sonication, those were dried by nitrogen gas flow and kept the substrates inside an incubator at 60°C. These dried substrates were used for thin-film deposition.

To deposit a thin film, a solution of the complex **1** was prepared at a concentration of 10 mg/ml in chloroform and dichloromethane mixture of a ratio of 1:1. The solution was ultra-sonicated for 3 hours to get a homogeneous mixture of the material. Enough amount of the solution was taken to make a thin film using spin coating at a speed of 4000 rpm and 1000 acceleration. The prepared film was dried on a hot plate at 70°C for 20 minutes. The film was characterized by an atomic force microscope (AFM) to get the surface morphology. Aluminum metal was deposited on the film using a thermal evaporation system at a base pressure of 10^{-6} mBar. The diameter of the Al contact was 500 μm. The schematic of the device is shown in Figure 3.1. The device was further characterized electrically to check the resistive memory property.

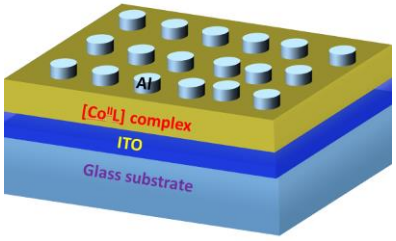

Figure 3.1 Schematic representation of the ITO/Co^{II}L/Al device.

3.3 Results and Discussion

3.3.1 Synthetic Aspects

The [Co^{III}L] complex, **1** was obtained by refluxing equal moles of LH_2, *9,9'-(Ethane-1,2-diylbis(azanediyl))bis(1H-phenalen-1-one),* and $Co(OAc)_2 \cdot 4H_2O$ in ethanol (Scheme 3.1). The complex **1** was isolated in the form of green precipitate from the reaction mixture, which on slow evaporation from Dichloromethane/Benzene (1:1) resulted in X-ray quality dark green block type crystals. The molecular structure of the complex was primarily confirmed by the single crystal X-ray diffraction (SCXRD) technique. Complex **1** was also further characterized by various techniques such as elemental analysis, HRMS, XPS, EPR, CV, UV-vis, and FT-IR spectroscopy (Figure 3.2) The thermal stability of the complex **1** (up to 230°C, Figure 3.2b) was confirmed with the thermogravimetric analysis (TGA). The good thermal stability of the complex can endure heat deterioration in the memory device. FT-IR spectrum of **1** (Figure 3.2a) shows the presence of characteristic ν(C=N) vibrational stretch at 1632 cm^{-1} and the ν(C-O)

stretching band at 1240 cm^{-1} [Chiang et al., 2014; Kanso et al., 2020]. HRMS analysis in positive ion mode shows a strong peak at m/z = 473.07 amu which corresponds to $[Co^{II}L]^+$ indicating complex **1** is stable in solution. The XPS-analysis for the cobalt 2p binding energies in the complex **1** is displayed in Figure 3.2c. For complex **1**, the main photopeak due to Co $2p_{3/2}$ appears at 779.44 eV and the comparatively half intense $2p_{1/2}$ level which splits into two peaks, appears at 794.40 and 795.90 eV. A similar splitting pattern was also observed by Burness et al. in a series of Schiff base Co(II) paramagnetic complexes [Burness et al., 1975]. Further, we have confirmed the paramagnetic behaviour of the **1** with the solid state EPR (g = 1.99) at room temperature (Figure 3.2e) [Chiang et al., 2014; Kanso et al., 2020].

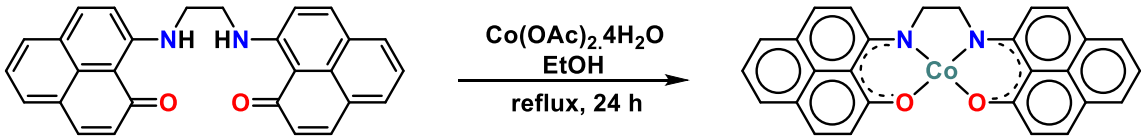

Scheme 3.1 Synthesis of the $[Co^{II}L]$ complex, **1**.

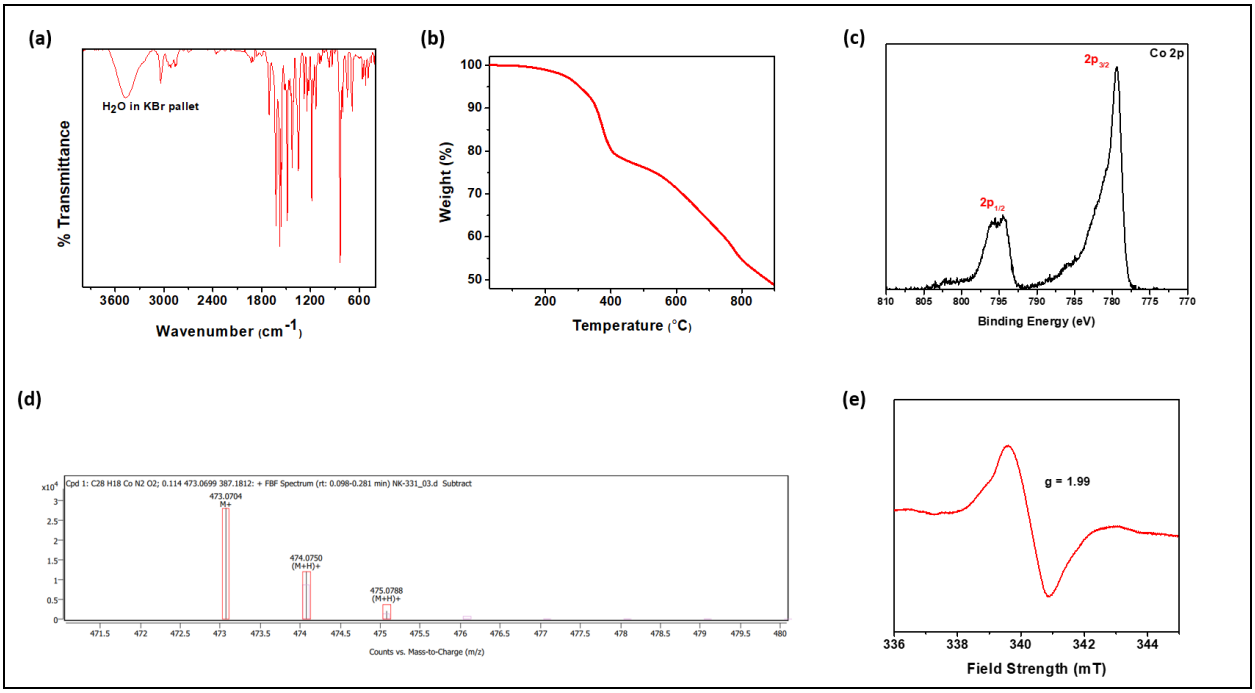

Figure 3.2 (a) FT-IR, **(b)** TGA, **(c)** Co 2p XPS, **(d)** HRMS, and **(e)** EPR spectra of the complex **1**.

3.3.2 Molecular and Supramolecular Structure of Complex 1

The crystal structure refinement parameters of the complex **1** are mentioned in Table 3.1. The molecular structure and coordination environment of **1** are depicted in Figure 3.3. The complex **1** crystalizes into the monoclinic $P2_1/c$ space group. The molecular structure of **1** shows that the Co(II) ion is present in the square planar geometry (τ4 = 0.037)[Pascualini et al., 2015; Yang et al., 2007] coordinated by the chelating bis-phenalenone ligand with *cis*-N2O2 donor set (O1, O2, N1, and N2 as the binding sites). The Co-N and Co-O bond distances observed in the complex **1**, [Co1-N1, 1.845(13) Å; Co1-N2, 1.847(13) Å] and [Co1-O1, 1.851(11) Å; Co1-O2, 1.839(11) Å] are comparable to that of the Co-N and Co-O bond distances [Co1-N1, 1.845(3) Å; Co1-N2, 1.853(3) Å] and [Co1-O1, 1.851(2) Å; Co1-O2, 1.842(2) Å] reported for the Co(II) salen complex. The O-Co-N bond angles in the present Co(II) complex [O2-Co1-N2, 93.869(5)°; O1-Co1-N1, 93.634(5)°] are also in close agreement with the bond angles values found in the Co(II) salen complex [O2-Co1-N2, 93.5 (2)°; O1-Co1-N1, 93.3(2)°] [Hiller et al., 1993].

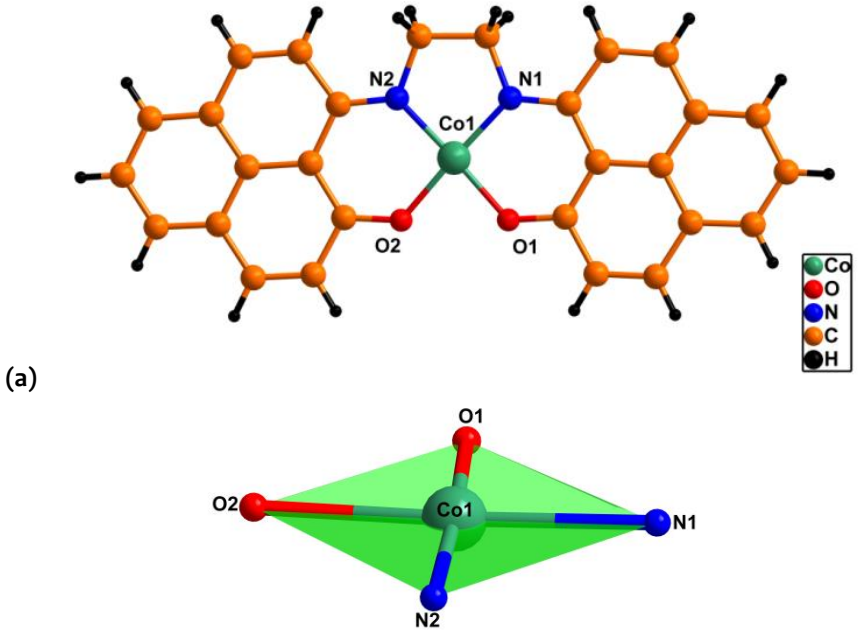

Figure 3.3 (a) Molecular structure, and **(b)** coordination environment around Co(II) center in complex **1**.

Table 3.1. Crystal data and structure refinement parameters for the complex **1** (CCDC 2150467).

Identification code	$[Co^{II}L]$ complex, **1**
Empirical formula	$C_{34}H_{24}CoN_2O_2$
Formula weight	551.51
Temperature/K	100
Crystal system	monoclinic
Space group	$P2_1/c$
a/Å	14.325(2)
b/Å	7.9315(12)
c/Å	21.786(3)
α/°	90
β/°	101.128(4)
γ/°	90
Volume/Å^3	2428.8(6)
Z	4
ρ_{calc}g/cm^3	1.5081
μ/mm^{-1}	0.744
F(000)	1141.8
Crystal size/mm^3	0.2 × 0.2 × 0.2
Radiation	Mo Kα (λ = 0.71073)
2Θ range for data collection/°	5.22 to 56.64
Index ranges	-19 ≤ h ≤ 19, -10 ≤ k ≤ 10, -29 ≤ l ≤ 29
Reflections collected	50984
Independent reflections	6035 [R_{int} = 0.0496, R_{sigma} = 0.0258]
Data/restraints/parameters	6035/0/352
Goodness-of-fit on F^2	1.072
Final R indexes [I>=2σ (I)]	R_1 = 0.0309, wR_2 = 0.0810
Final R indexes [all data]	R_1 = 0.0397, wR_2 = 0.0903
Largest diff. peak/hole / e Å^{-3}	0.43/-0.42

The closer inspection of the unit cell of **1** reveals the presence of four molecules per unit cell [Figure 3.4a] interacting with one another through the C–H···O, C–H···N, as well as π···π

stacking interactions. The two planar molecules in the complex interact through the classical C27─H27a···O1 (3.218 Å) and C28─H28b···N1 (3.338 Å) hydrogen bonding interactions, generating a linear zig-zag one-dimensional supra-molecular pattern which is further stabilized by the π···π stacking (3.723, 3.763 and 3.801 Å) between the planar aromatic rings of phenalenyl unit of the ligand (L), respectively (Figure 3.4b). Interestingly, we have observed two different non-classical [Chandrasekhar et al., 2013; Gopal et al., 2014; Yusuf et al., 2021] intermolecular hydrogen-bonding (C─H···O) patterns between the oxygen atom of one molecule with aromatic hydrogen atoms of the phenalenyl ring (C11─H11···O1, 2.964 Å; C9─H9···O2, 3.403 Å) of another molecule. Also, the π···π stacking has procreated and stabilized the Z-shape spatial arrangement of the molecules in the supramolecular assembly of the complex **1** (Figure 3.4c). The extension of π···π interactions in two dimensions generated a 2D assembly structure (Figure 3.4d) which is similar to the π···π stacking present in the TTF/TCNQ (tetrathiafulvalene/tetracyanoquinodimethane), a well-known charge transfer salt [Alves et al., 2008; Chernenkaya et al., 2015; Chi et al., 2002; Kirtley et al., 2008; Sekine et al., 2017].

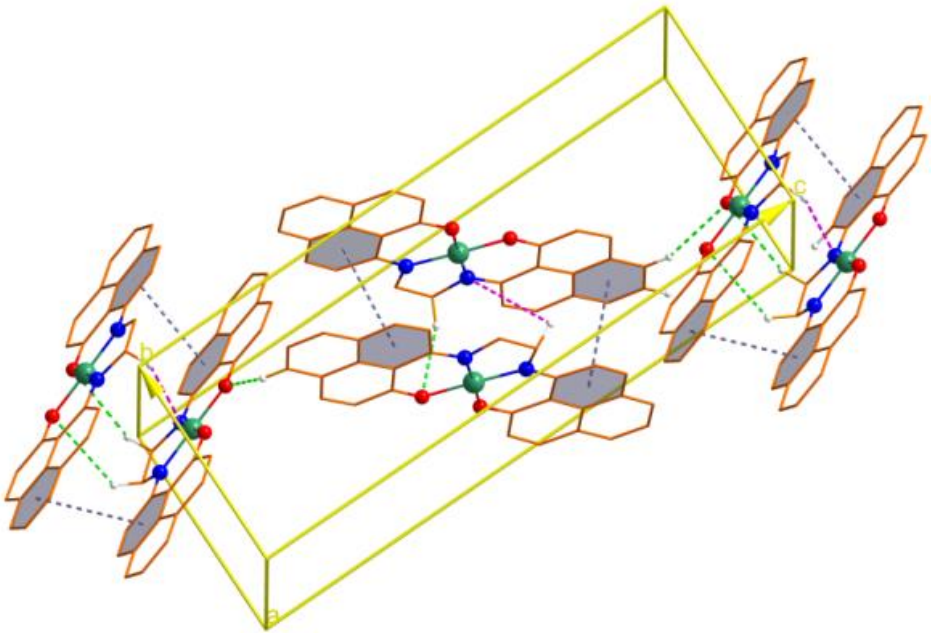

(a)

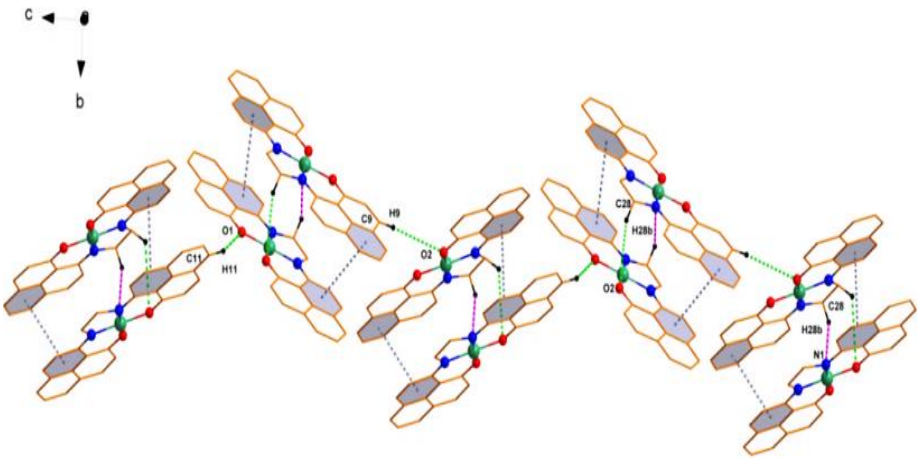

(b)

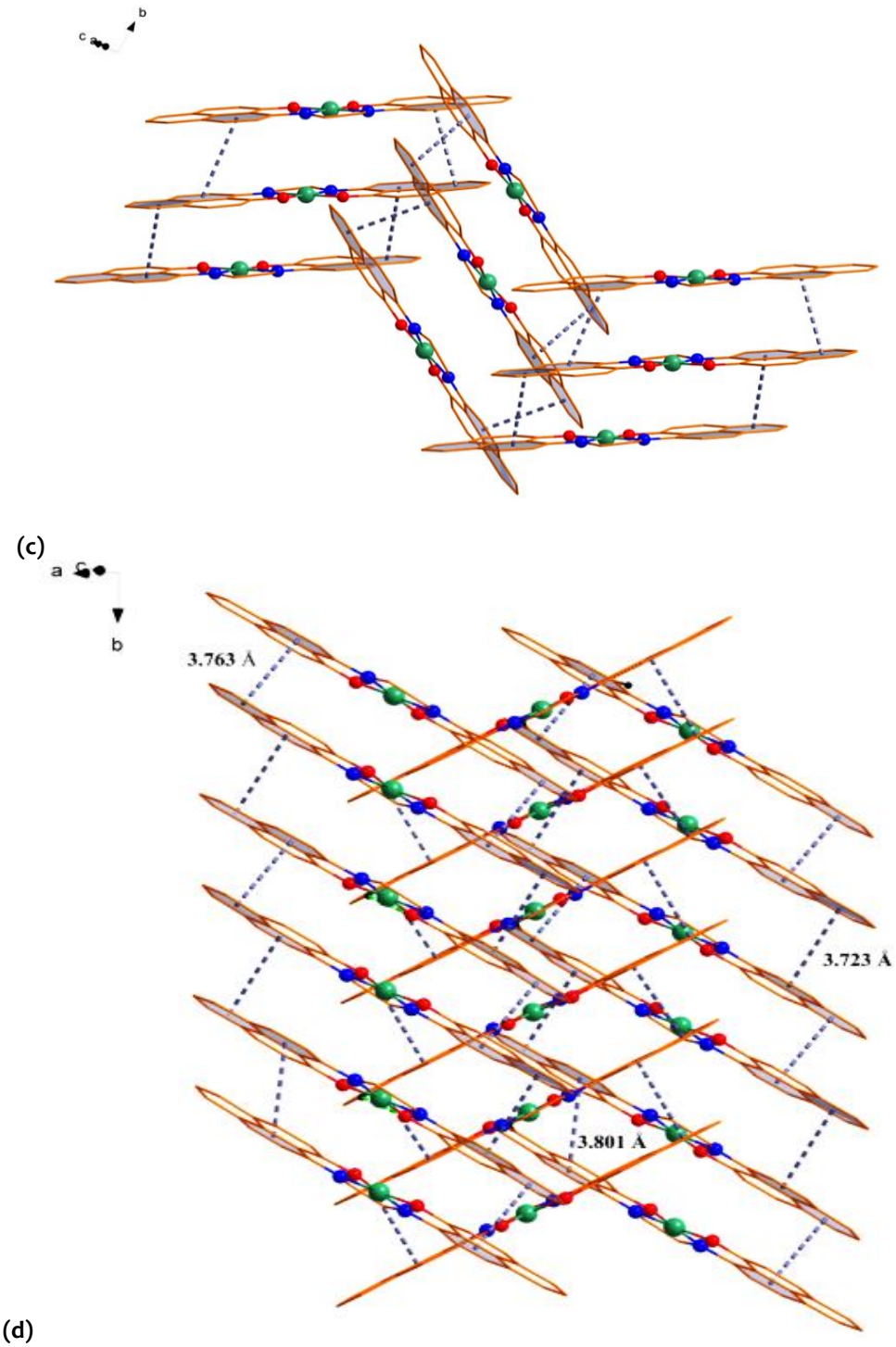

Figure 3.4 (a) Unit cell of complex **1** displaying the non-covalent (C—H···O, C—H···N, and π···π) interactions. **(b)** Infinite one-dimensional zig-zag pattern of **1** along the a-axis: Bond parameters; C27—H27a···O1, 3.218 Å; C28—H28b···N1, 3.338 Å; C11—H11···O1, 2.964Å; C9—H9···O2, 3.403 Å (hydrogen atoms are not displayed for the clarity except for those participating in hydrogen bonding). **(c)** The phenalenyl rings in planar complex **1** involved in the π···π stacking forming a Z-shape orientation in one-dimension. **(d)** Two-dimensional supramolecular framework of complex **1**.

3.3.3 Photophysical studies

The UV-visible spectrum of the complex **1** consists of four distinct bands in the visible region (621 nm, 571 nm, 476 nm, and 347 nm) and the wavelength corresponding to stronger photon absorption, λ_{max} appeared in the UV region at 285 nm (Figure 3.5). To obtain further insights into the nature of each electronic transition, scalar relativistic TD-DFT calculated transitions

were computed in collaboration for the complex **1**. Figure 3.5a shows the experimental and simulated absorption spectra. The dominant molecular orbital representations of each TD-DFT calculated transition in CH_2Cl_2 solvent are depicted in Figure 3.5b. The calculated low-lying NIR(Near Infrared) peaks at 1430 and 854 nm can be described as transitions from *β*-HOMO → *β*-LUMO and *β*-HOMO → *β*-LUMO+1 [78%], *α*-HOMO-1 → *α*-LUMO [12%], respectively with MLCT/LLCT character (Figure S7). A very weak absorption peak observed at 758 nm/1.634 eV corresponds to *α*-HOMO → *α*-LUMO transition with a mixed character of MLCT/LLCT. The first prominent intense broad band observed in the experimental spectrum at 621 nm corresponds to an excited state that largely consists of *α*-HOMO-1 → *α*-LUMO [33%], *α*-HOMO-2 → *α*-LUMO+1 [28%] and *β*-HOMO-2 → *β*-LUMO+2 [18%] electronic transitions with MLCT character. A weak absorption band localized at 571 nm is appeared blue-shifted in the computed spectrum at 565 nm and primarily associated with charge transfer from phenalenyl ligand to the central metal ion [*β*-HOMO-3 → *β*-LUMO]. The second prominent intense absorption band that appeared at 447 - 476 nm in the recorded spectrum is partially attributed to charge transfer from filled π orbitals to vacant π* orbitals of ligand (LLCT). Whereas the high-lying intense absorption peak at 347 nm is described by electronic transitions with mixed LLCT/LMCT/MLCT character and involves two dominant transitions; *α*-HOMO → *α*-LUMO + 6 and *β*-HOMO – 8 → *β*-LUMO + 1. Unlike the experimental spectra, where an intense peak is observed near 476 nm, the TD-DFT calculation of the monomer complex depicted a weak broad absorption band in the wavelength range of 380 – 550 nm. To investigate this further, TDDFT calculation is carried out for an optimized π···π stacked dimer of complex **1**. The theoretical computed spectrum of the dimer displays an intense peak near 507 nm with significant intermolecular charge transfer character, shown in Figure 3.5c. Interestingly, the low-energy absorption peaks of the dimer complex show substantial contributions from inter-molecular CT. As a result, a notable difference is observed between the experimental recorded and theoretical computed (monomer) spectra for low-lying excitations (400 – 800 nm). It is worth mentioning that a High-Spin (HS) and a "Broken-Symmetry" Low-Spin (BSLS) approach are considered, and no distinguishable difference is observed between the two computed spectra of π···π stacked dimer complex. The TD-DFT calculation in the BSLW approach is carried out by constructing opposed spin densities on the metal ions. The HS-BSLS energy difference is found to be 12.19 cm^{-1}, which implies a very weak anti-ferromagnetic coupling (-12.23 cm^{-1}) between two metal ions.

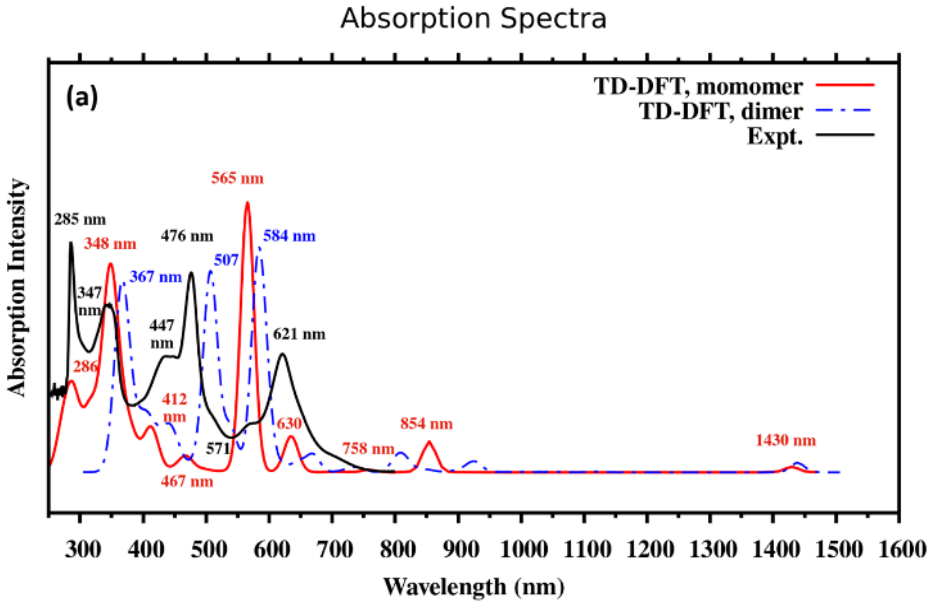

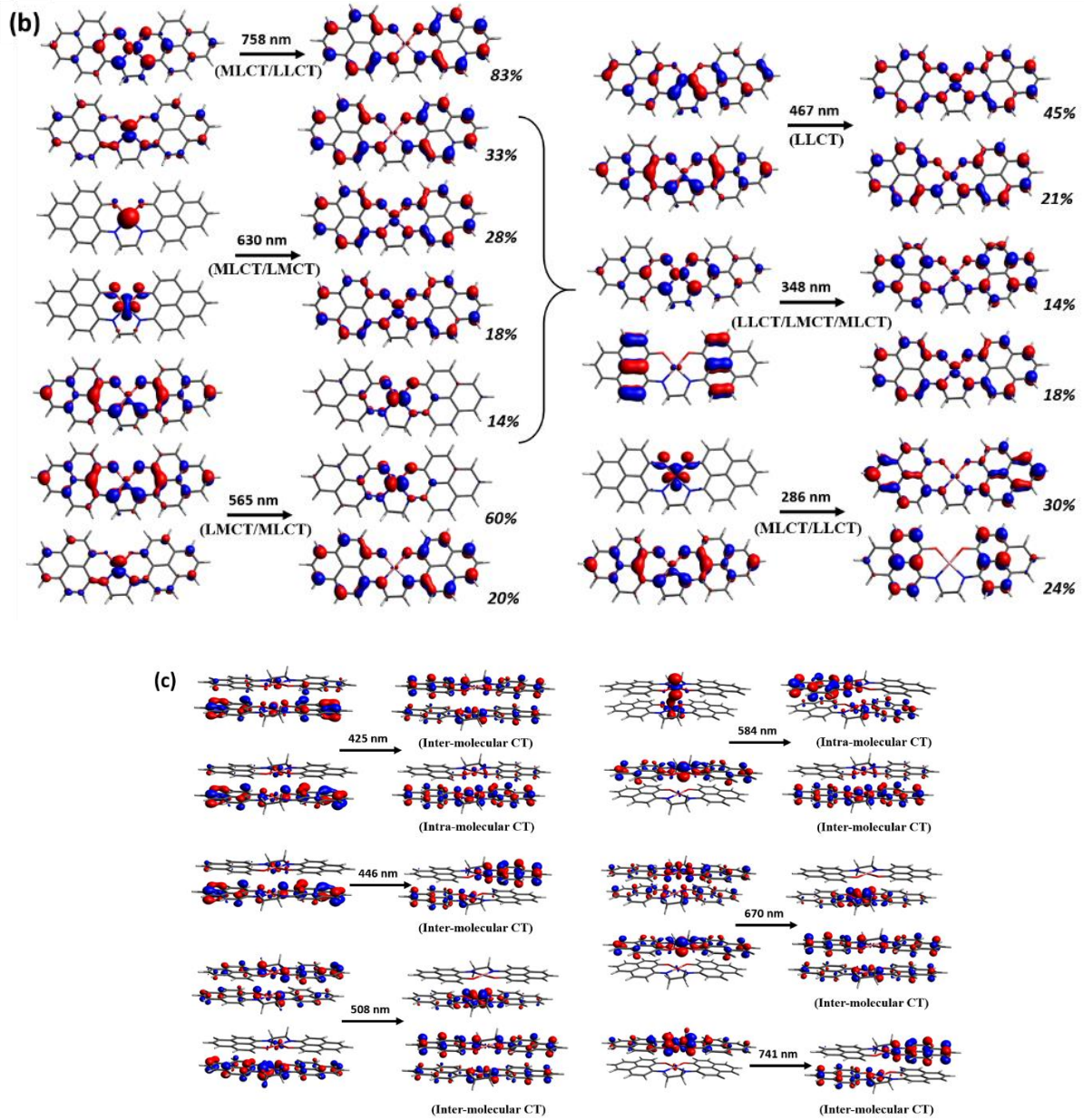

Figure 3.5 (a) Computed absorption spectrum of complex **1** using the TD-DFT calculations. The experimental spectrum of the complex is shown in a black solid line for comparison. The molecular orbital representations of electronic transitions corresponding to the TD-DFT computed absorption spectrum of **(b)** the monomer **1** complex; and **(c)** the π···π stacked dimer Co-complex (*S* = 0) in DCM solvent. A contour value of 0.04 au is used to generate the plots.

3.3.4 Resistive memory device behaviour

Electrical characterizations of the device obtained from the complex **1**, ITO/Co^{II}L/Al, has been performed in collaboration by a homemade probe station and Keithley 4200-SCS semiconductor analyzer. The current-voltage (I-V) characteristics are shown in Figure 3.6a. The current changes are measured at particular voltage iteration, and at a 1.5-volt iteration the device has obtained stable I-V characteristics. Voltage iterations are taken from -1.5 V to 1.5 V. The applied voltage starts from -1.5 V, increases to 0 V and again increases to 1.5 V, followed by a voltage sweep back to -1.5 V (the corresponding current is shown by cyan arrows). At -1.5 V, the conducting state of the device is high, which means the device is in a low resistance state(LRS). At the positive voltage side the current switches to a low conducting state or high resistance state(HRS). Again at the small negative bias, the current went to a high conducting state, as

shown on the negative bias side of Figure 3.6a. 1st, 10th, and 20th iterative cycles depicted here show two different resistive states on the positive bias side.

The stability of the resistive memory device is checked by applying a particular voltage called read voltage. The device obtained from the complex **1** is called a resistive memory device because it can memorize its resistance state after and before the writing process. We have checked its data retention capability after performing various write and erase cycles. For this device, a writing voltage of -1.5 V and erasing voltage of 1.5 V are applied for 10 seconds each. According to the I-V characteristics, when the write voltage is applied the device should be in LRS, and when the erase voltage is given the device should be in HRS. A read bias of 0.3 V is applied to check the two different resistive states. Figure 3.6c shows the two different resistance states for more than 2000 seconds.

The random access memory(RAM) property of the device has been realized from the write-read-erase-read cycle. For this, a write, erase and read voltage of -1.5 V, 1.5 V, and 0.3 V is applied for 10 seconds each. After applying -1.5 V, the device went to LRS and when reading by applying a read voltage it showed LRS. Again erase bias of 1.5 V applied and when read the state by applying read voltage then it shows HRS. The write-read-erase-read cycle is taken more than 200 times and it shows two different resistance states indicating the device can be used as RAM.

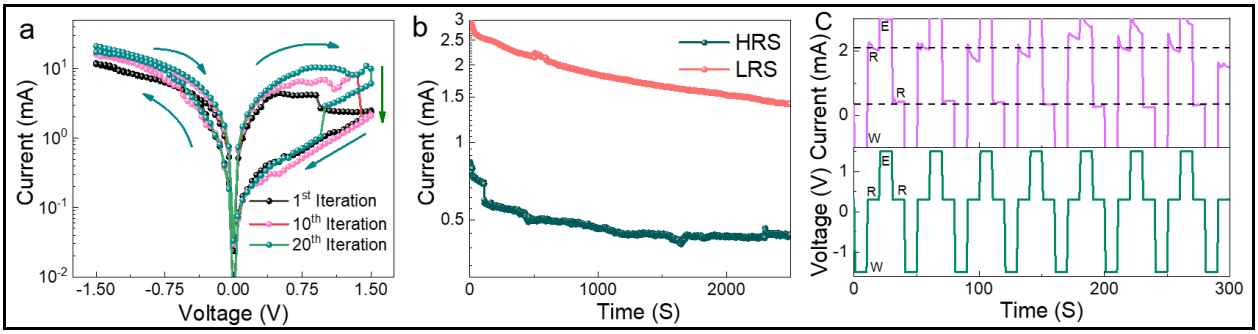

Figure 3.6 (a) The current-voltage characteristics of the device are taken from -1.5 V to 1.5 V. The cyan colour arrows show the current path with applied voltage. **(b)** The retention of two different resistance states or current states is shown. More than 2000 seconds of retention is checked and the device shows two different resistance states. **(c)** The RAM properties of the ITO/Co^{II}L/Al device are also shown in this figure. At a particular voltage (0.3 V) the device shows two different resistive states after the read and erases process.

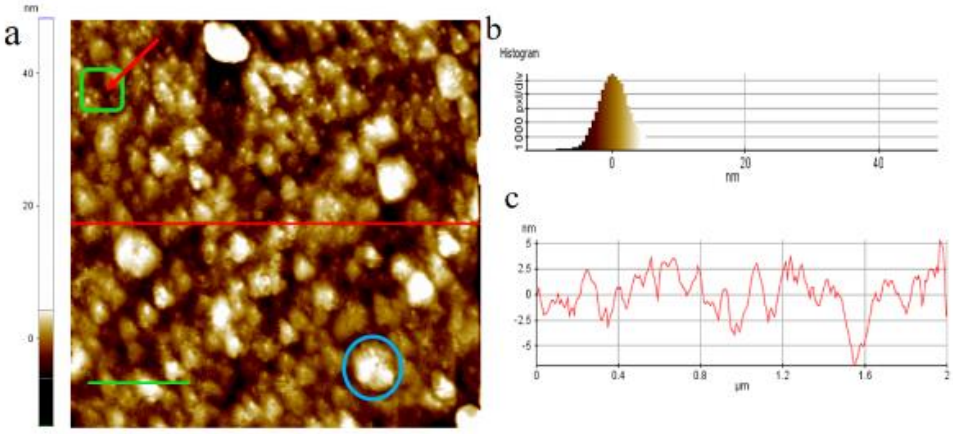

Figure 3.7 (a) AFM image of the deposited thin-film on an area of 2×2 µm². The scale shows a length of 0.5 µm. **(b)** The area histogram displays the roughness of the whole area. **(c)** The line profile shows the roughness along a particular line marked by the red colour on the image.

The surface morphology of the thin-film is studied using a park system (XE-70) atomic force microscope. Non-contacting AFM mode is applied with the NCST-Au tip. A scan rate of 0.75 lines per second is applied and the tip is kept at a fixed distance of 12 nm. The image of area 2×2 μm^2 is shown in Figure 3.7a and the clusters on the film are shown by cyan coloured circle. The RMS, roughness of the surface is 3.32 nm and the average surface roughness is 2.35 nm of the thin film. Further details can be found in the surface histogram picture and line profile of the image, as shown in Figures 3.7b and Figure 3.7c, respectively. The histogram is showing a Gaussian distribution of roughness. The line profile along the line as indicated by the red colour on the image, shows the height profile.

3.3.5 CV, DFT Studies, and Mechanistic Details

The redox behaviour of the complex **1** is studied using the cyclic voltammetry technique. The CV experiments are carried out in DMF solvent consisting of the three electrodes cell with tetrabutylammonium hexafluorophosphate ($TBAPF_6$) as the supporting electrolyte. As shown in Figure 3.8, the cyclic voltammogram of the complex **1** consists of two quasi-reversible reduction waves at -1.17 V (ΔE_1 = 90 mV) and -0.99 V (ΔE_2 = 65 mV), respectively, which can be accounted for the successive ligand based reductions which are well known for the phenalenyl-based metal complexes [Das et al., 2019b]. The quasi-reversible oxidation wave at +0.22 V (ΔE_3 = 70 mV) vs Ag/AgCl (3.0 M KCl) reference electrode can be assigned to the Co^{3+}/Co^{2+} redox couple [Chai et al., 2014; Tang et al., 2017]. By utilizing the ferrocenium/ferrocene couple ($FeCp_2^{+/0}$)[Pan et al., 2013] as the internal reference, the absolute $HOMO_2$, $HOMO_1$, and $LUMO_1$, $LUMO_2$ energy levels of the complex **1** are estimated to be -5.25, -4.51, and -3.60, -2.86 eV, respectively.

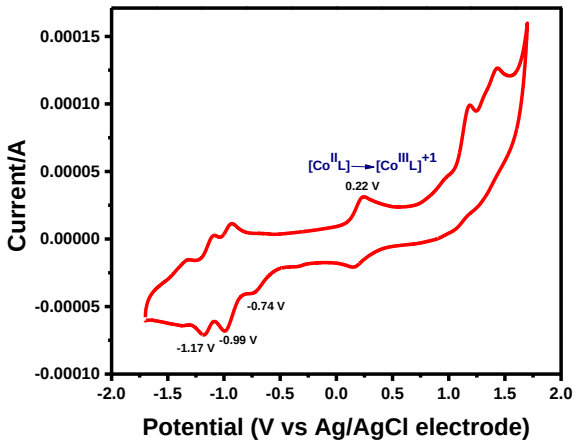

Figure 3.8 CV of the complex **1** at a scan rate of 500 mV/s acquired using a Pt working electrode, Pt-wire counter electrode and Ag/AgCl (3.0 M KCl) reference electrode.

On the other hand, the unrestricted DFT calculation performed in collaboration using BP86 functional suggests that the natural spin density (Table 3.2) calculated for the paramagnetic complex **1** is predominantly localized on the metal center (~ 87% of the total spin population), as depicted in Figure 3.9a. This concludes that the redox processes are localized prevailingly on the metal center. The spin density of the open-shell metal complex in its doublet state has a shape very similar to the β-LUMO of the complex. Here, the β-LUMO represents a singly unoccupied molecular orbital (SUMO) in classical MO representation. In addition, the β-LUMO has the largest spatial overlap with the α-HOMO, where α-HOMO is associated with a singly occupied molecular orbital (SOMO). Therefore, the open shell for **1** can be straightforwardly attributed either to α-HOMO (as SOMO) or to β-LUMO (as SUMO). The molecular orbitals are computed at the BP86+D3BJ/def2-TZVPP level of theory. The spin-orbital α-HOMO-1 has the exact spatial shape as that of the spin-orbital β-HOMO and thus can be assigned as a doubly

occupied highest energy molecular orbital (HOMO, in a conventional way). Similarly, *α*-LUMO and *β*-LUMO+1 spin-orbitals form a doubly unoccupied lowest energy molecular orbital (LUMO, in a conventional way). The energy difference between these two MOs (SOMO and LUMO) is found to be 1.59 eV which is in good accord with the value (1.65 eV) obtained from the measured UV-vis spectrum (Figure 3.9c). The computed MO energy values are -5.01, -4.96, -4.70, -3.11, and -2.99 eV for *α*-HOMO-2, *α*-HOMO-1, *α*-HOMO, *α*-LUMO, *α*-LUMO+1, respectively, the MOs are demonstrated in Figure 7(b). Similarly, MO energy for *β*-HOMO-1, *β*-HOMO, *β*-LUMO, *β*-LUMO+1, and *β*-LUMO+2 MOs are -4.61, -4.52, -3.55, -3.10, and -2.89 eV, respectively. The BP86 computed MO energy values are consistent with the energy values derived from the electrochemical studies. Following the theoretical analysis of spin-density distribution and localized molecular orbitals, it can be concluded that the redox processes are localized on central metal ion $Co^{(II)}$ and readily forms $Co^{(III)}$ upon the first oxidation of the metal complex. The calculated relative electrode potential (E°) for the oxidation step appears at +0.16 V, as referenced to the Ag/AgCl (3.0 M KCl) electrode. Our theoretical observation is coherent with the CV results, where the first oxidation peak appeared at an on-set potential of +0.09 V (peak potential +0.22 V) and is associated with the metal ion oxidation [$Co^{(II)} \rightarrow Co^{(III)}$] of the complex **1**. Analogously, the first reduction can be imputed as a metal ion reduction [$Co^{(II)} \rightarrow Co^{(I)}$] of the complex **1**, as the unrestricted DFT calculation shows that the electron density on the *β*-LUMO has significant metal contribution (nearly 65%). However, the DFT calculation also reveals that the *β*-LUMO also has nearly 35% ligand contribution, and thus, a ligand-based reduction cannot be completely excluded. The doubly unoccupied LUMOs which are predominantly localized on ligand moieties are responsible for ligand-based reduction at further potentials. The NBO analysis showed that in the metal complex, the metal ion coordinates to nitrogen and oxygen atoms of the ligand moiety through electron donation from the lone pairs on the nitrogen and oxygen atoms to *s* and *d* orbitals on the metal ion (Table 3.3). The stabilization energy associated with these ligand-to-metal donor-acceptor interactions are: ~ 19 - 46 kcal/mol [N(LP)→Co(LP*)], 4 - 7 kcal/mol [O(LP1)→Co(LP*)] and 16 - 39 kcal/mol [O(LP2)→Co(LP*)]. Whereas the NBO-NBO* interactions of a ligand-to-ligand and metal-to-ligand lie in the range of 10 – 25 kcal/mol and 1- 3 kcal/mol, respectively. Following the NBO analysis, one can conclude that the LMCT and LLCT play a significant role in the complex **1**. Detailed discussion on the NBO analysis of the complex is given in the Supporting information. The geometry optimization of the square-planar Co-complex in a quartet spin state results in an SCF convergence failure. The final geometry shows a huge distortion from the square planar geometry. The optimization involves a very high energy process according to our theoretical calculations. Therefore, the possibility of the square-planar complex **1** in a quartet spin state is discarded in the present scenario.

Table 3.2 The natural population analysis (NPA) charges (au) and spin density on metal and its neighbouring coordinated atoms.

Atom	*Formal Oxidation State*	*Natural Charges (e)*	*Natural Spin Density*
Co	+2	+0.8712	0.8716
N1	-1	-0.4375	0.0414
N2	-1	-0.4375	0.0415
O1	-2	-0.5591	0.0410
O2	-2	-0.5591	0.0410

The memory effects of the ITO/Co^{II}L/Al device can be closely correlated with the redox activity of the central metal ion. In a forward bias condition, i.e., ITO at positive and Al at negative bias, the hole injection barrier (0.25 eV) of ITO/$HOMO_1$(~SOMO) interface is relatively small than the electron injection barrier (0.58 eV) of Al/$LUMO_1$(~SUMO) interface, indicates that **1** is a p-type material with holes as the dominant charge carrier. The device operating mechanisms at

three different forward voltage biases are shown in Figure 3.10. With the increase in positive voltage bias, the applied electric field exceeds the hole injection barrier and the device switches to a LRS or equivalent to ON-state at very low voltage. As discussed above, the redox-active site for oxidation is localized on the central metal ion. Thus oxidation of $Co^{(II)}$ to $Co^{(III)}$ near the interface initiates the device and holes are injected into the $HOMO_1$ (ON-state). With a further increase in the forward bias, holes (charge carriers) are migrated through the π-conjugated backbone [Li et al., 2019] of the ligand and transported from ITO/material interface to Al/material interface. At the positive voltage V > 0.75 V, the applied electric field exceeds the electron injection barrier; as a result, electrons are injected from the Al electrode to $LUMO_1$. Since $LUMO_1$ is predominantly situated on metal-ion, an injection of an electron into it neutralizes the hole. As a result, the total count of charge carriers starts diminishing. With further increasing the voltage, the device subsequently switches to High Resistance State (HRS) or equivalent to "OFF-state" during the first iteration. During the reverse bias voltage, the hole injection barrier (-0.25 eV) of the Al/$HOMO_1$ interface is relatively small than the electron injection barrier (1.08 eV) of the ITO/$LUMO_1$ interface, suggesting that the hole injection is energetically more favourable than the electron injection. At voltage V ~ -1.5 V, the applied electric field exceeds the hole injection barrier and thus the device is in its "ON-state". This can be regarded as the "writing" process in a memory device. The device remains in the LRS even after the power is turned off.

Table 3.3 Second-order perturbation energy E_2 (kcal/mol), off-diagonal Fock matrix elements $F(i,j)$ and acceptor – donor energy values $(E_j - E_i)$ (a.u.) of selected donor-acceptor NBO-NBO* interactions in metal-complex, as computed at UKS BP86+D3/TZVPP method.

Donor-Acceptor	***α – spin-orbital***			***Donor-Acceptor***	***β – spin-orbitals***		
	E_2	$E_j - E_i$	$F(i,j)$		E_2	$E_j - E_i$	$F(i,j)$
LP(1)$O_{1,2}$ – LP(1)Co*	5.32	0.23	0.045	LP(1)$O_{1,2}$ – LP*(1)Co	4.66	0.25	0.043
LP(1)$O_{1,2}$ – LP(2)Co*	6.62	0.63	0.081	LP(1)$O_{1,2}$ – LP*(3)Co	6.27	0.62	0.079
LP(2)$O_{1,2}$ – LP(1)Co*	38.51	0.13	0.090	LP(2)$O_{1,2}$ – LP*(1)Co	33.03	0.17	0.093
LP(2)$O_{1,2}$ – LP(2)Co*	16.16	0.53	0.116	LP(2)$O_{1,2}$ – LP*(3)Co	16.44	0.54	0.119
LP(1)$N_{1,2}$ – LP(1)Co*	45.62	0.12	0.095	LP(1)$N_{1,2}$ – LP*(1)Co	40.27	0.15	0.097
LP(1)$N_{1,2}$ – LP(2)Co*	19.40	0.52	0.126	LP(1)$N_{1,2}$ – LP*(3)Co	19.23	0.52	0.126
LP(4)Co – π(N – C)*	1.66	0.15	0.020	π(O – C) – LP*(2)Co	2.41	0.17	0.026
LP(3)$O_{1,2}$ – π(C – C)*	25.67	0.24	0.099	π(N – C) – LP*(2)Co	3.10	0.14	0.027
π(C – C) – π(N – C)*	14.63	0.19	0.066	LP(3)Co – π*(N – C)	2.48	0.12	0.022
π(C – C) – π(C – C)*	10.01	0.22	0.060	LP(3)Co – π*(O – C)	1.69	0.12	0.018
				LP(1)C – π*(C – C)	42.15	0.11	0.084
				π(C – C) – π*(O – C)	14.91	0.18	0.066

				π(C – C) – π*(N – C)	12.82	0.19	0.062

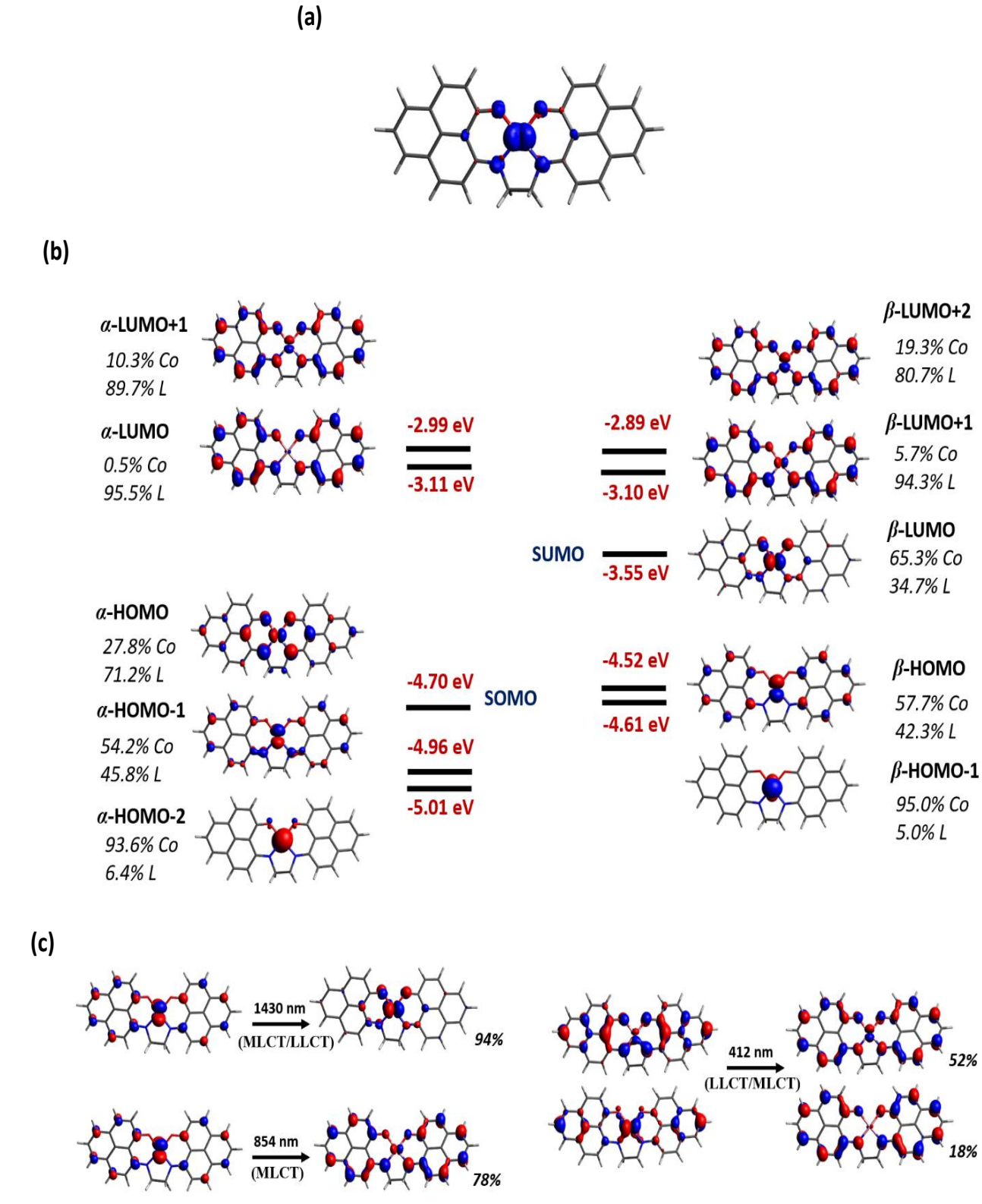

Figure 3.9 (a) Spin density of complex **1** at 0.0035 au (e^2/bohr^4) isosurface value (blue, α spin; red, β spin density). **(b)** BP86 computed molecular orbitals of the Co-metal complex, **1** are plotted with an isosurface value of 0.04 au. **(c)** The MO energy and the metal-ligand composition of the respective MO are also given. The molecular orbital representation of electronic transitions corresponding to the TD-DFT computed absorption spectrum of complex **1** at 1430, 854 and 412 nm peaks. The contour value used to generate the plots is 0.04 au.

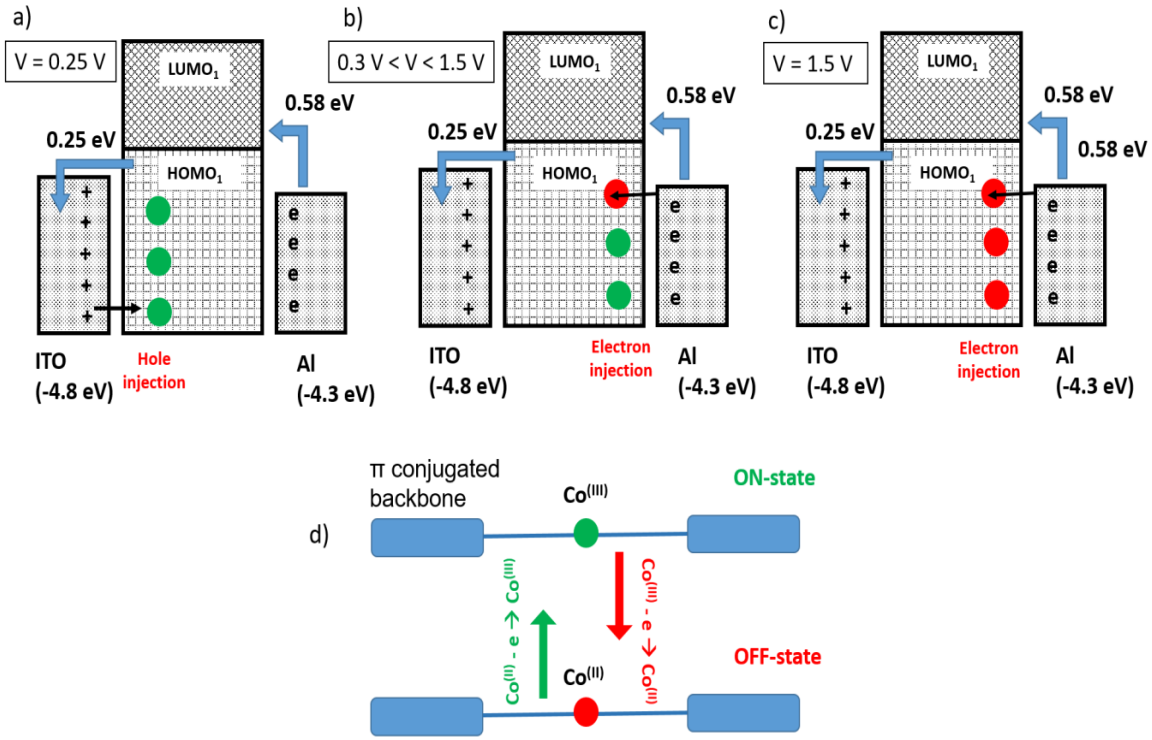

Figure 3.10 Schematic diagram of a memory device operating plausible mechanism during forward voltage bias at **(a)** V = 0.25 V, **(b)** 0.3 V < V < 1.5 V, and **(c)** V = 1.5 V. **(d)** Metal-based redox process controls the memory device mechanism.

3.4 Summary

A square planar [Co^{II}L] complex, **1** is synthesized using redox active phenalenyl-derived ligand, LH_2 = *9,9'-(Ethane-1,2-diylbis(azanediyl))bis(1H-phenalen-1-one)*. The molecular structure of the **1** reveals the presence of π···π stacking analogous to the one present in TTF/TCNQ charge transfer salt. The random access memory (RAM) property of the device fabricated using the complex **1** as an active material has been studied from the write-read-erase-read cycle, where the device has interestingly shown two different resistance states for > 2000 seconds with an on/off ratio > 10^2 at 0.3 V. DFT + TDDFT and electrochemical studies have revealed the possibility of a redox switching mechanistic pathway where the p-type complex **1** can initiate the switching with hole injection from the ITO electrode. The redox reaction at the Co^{II} metal center and the charge carrier π-conjugated backbone of the ligand can provide a medium for the hole transportation from ITO/material interface to Al/material interface.

…